Direct Observation of Wave-coherent Pressure Work in the Atmospheric Boundary Layer

Seth F. Zippel [1]*, James B. Edson [1], Malcolm E. Scully [1], Oaklin R. Keefe[1]

[1]266 Woods Hole Rd., Woods Hole MA 02543

Key Points:

- Measurements of wave-coherent energy fluxes are reported via pressure vertical-velocity cospectra
- Measured pressure work cospectra are consistent with an existing simple model based on wave growth rate parameterizations
- Wave-coherent pressure work energy fluxes reached nearly 0.2 W m^{-2} during an energetic wind event

*266 Woods Hole Rd., Woods Hole MA 02543

Corresponding author: Seth F. Zippel, szippel@whoi.edu

Abstract

Surface waves grow through a mechanism in which atmospheric pressure is offset in phase from the wavy surface. A pattern of low atmospheric pressure over upward wave orbital motions and high pressure over downward wave orbital motions travels with the water wave, leading to a pumping of kinetic energy from the atmospheric boundary layer into the waves. This pressure pattern persists above the air/water interface, modifying the turbulent kinetic energy in the atmospheric wave-affected boundary layer. Here, we present field measurements of the transfer of energy from wind to waves through wave-coherent atmospheric pressure work. Measured pressure work cospectra are consistent with an existing model for atmospheric pressure work. Measured pressure work energy fluxes reach 0.1-0.2 W m^{-2} during the largest measured wind event (winds reaching 16.5 m s^{-1}). The implications for these measurements and their importance to the turbulent kinetic energy budget are discussed.

Plain Language Summary

Surface waves grow through a pattern of atmospheric pressure that travels with the water wave, acting as a pump against the water surface. The pressure pumping, sometimes called pressure work, or the piston pressure, results in a transfer of kinetic energy from the air to the water that makes waves grow larger. To conserve energy, it is thought that the pressure work on the surface must extract energy from the wind speed or wind turbulence that would otherwise be able to make the wind faster, or that sets the shape of the wind profile with height. In this paper, we present direct measurements of pressure work in the atmosphere above surface waves. We show that the energy extracted by atmospheric pressure work fits existing models for how waves grow, and a simple model for how waves reduce energy in the turbulent kinetic energy budget. To our knowledge, these are the first reported field measurements of wave-coherent pressure work.

1 Introduction

The problem of airflow over surface gravity waves is old, with an ongoing record of publications on the topic that started nearly 100 years ago (Jeffreys, 1924, 1925; Miles, 1957; Phillips, 1957; Janssen, 1991; Belcher & Hunt, 1993; Hristov et al., 2003; Ayet & Chapron, 2022). A nuanced understanding of both the growth of waves, and the statistics of atmospheric variables is continuing to evolve (Pizzo et al., 2021), which combines

multiple existing theories over different regimes. A common central theme in wind-over-wave theories is the role of out-of-phase atmospheric pressure on the sea surface, which leads to the growth of surface waves. Surface wave growth requires a flux of energy, which must be balanced by a loss of kinetic energy from the atmosphere.

Following many previous studies (e.g., Hara & Belcher, 2004, Equation 38 therein, Cifuentes-Lorenzen, Edson, & Zappa, 2018, Equations 2-3 therein, Ayet & Chapron, 2022, Equation 22 therein) the Turbulent Kinetic Energy (TKE) equation in the atmosphere above growing surface waves can be posed as

$$\tau_{tot} \cdot \frac{d\langle u \rangle}{dz} + \frac{d}{dz}\Pi_w - \epsilon = 0, \tag{1}$$

where buoyancy has been assumed neutral, the turbulent (wave-incoherent) pressure and energy transport terms are assumed to cancel, $\tau_{tot} = -\rho_a \langle u'w' \rangle$ is turbulent stress, Π_w is the wave-induced KE transport, and ϵ is the TKE dissipation rate. Here, $\langle \cdot \rangle$ represents a time average, $u' = u - \langle u \rangle$ is the fluctuating horizontal velocity, and w' is the fluctuating vertical velocity. Turbulent fluctuations can be decomposed into the into wave-coherent, and wave-incoherent components such that $w' = \tilde{w} + w'_t$. The wave-induced KE transport is defined $\Pi_w = -\langle \tilde{p}\tilde{w} + \rho_a \tilde{u}\tilde{u}\tilde{w} \rangle$ is comprised of the pressure work, $\langle \tilde{p}\tilde{w} \rangle$, and a triple velocity product[1]. When evaluated at the surface, the wave-coherent pressure work, $\langle \tilde{p}\tilde{w} \rangle(z = 0)$, is largely responsible for the growth of surface waves (although recent work by M. Buckley, Veron, & Yousefi, 2020 has shown the importance of wave-coherent viscous stresses at lower energy conditions).

The energy equation is important for understanding how the wind-wave growth feeds back to atmospheric turbulence, which can modify turbulent statistics and the mean wind profile from classic rigid boundary layer results. As discussed in Ayet and Chapron (2022), the choice of turbulent closure schemes in 2-equation turbulence models for airflow over wind waves results in different profiles for ϵ and $\langle u \rangle$ (Ayet & Chapron, 2022 Figure 5 therein). While there are many existing field measurements of stress, mean winds, and TKE dissipation rate over the open ocean, there are (to the authors' knowlege) no reported field

[1] We note there is some difference in how the triple velocity product is treated in previous work. Since the focus of this work is the pressure term, not the triple velocity product, we opt for the definition used in Ayet and Chapron (2022) and note the differences here

measurements of wave-coherent pressure work which serves as the mechanistic link between the downward flux of energy that makes waves grow, and the loss of energy from atmospheric turbulence.

1.1 Pressure work Model

Janssen (1999) developed a simple model for wave-coherent atmospheric pressure work $\langle \tilde{p}\tilde{w} \rangle (z)$, which was posed as a function of the wave growth rate $\beta(f, \theta)$, the surface wave energy spectrum, $E(f, \theta)$, and a vertical decay rate, $\exp(-2kz)$,

$$\langle \tilde{p}\tilde{w} \rangle (z) = -\int\int S_{in}(f,\theta) e^{-2kz} d\theta df = -\int\int \beta(f,\theta) E(f,\theta) e^{-2kz} d\theta df, \tag{2}$$

where S_{in} is the spectral wind to wave energy flux, k is the frequency-dependant wavenumber assumed to follow the linear dispersion relation, f is the frequency, θ is the relative direction between wind and waves, and z is height above the mean water level.

Plant (1982) fit numerous existing wave growth data sets, finding a growth rate of

$$\beta(f,\theta) = (0.04 \pm 0.02) \frac{u_*^2}{c^2} \omega \cos(\theta), \tag{3}$$

where u_* is the atmospheric friction velocity, $\omega = 2\pi f$ is the radian frequency, and $c = \omega/k$ is the frequency-dependant wave phase. Janssen (1989, 1991) showed that the drag over the water depends on sea state, which in turn modifies the growth rate. The new proposed growth rate was,

$$\beta(f,\theta) = B \frac{\rho_a}{\rho_w} \frac{u_*^2}{c^2} \omega \cos^2(\theta), \tag{4}$$

where B is the so-called Miles constant which is a function of the non-dimensional critical height, and fraction of wave to total stress $\tilde{\tau}/\tau_{tot}$. Computation of B is often achieved through iteration as described in Komen et al., 1996.

In this work, we present direct covariance measurements of wave-coherent pressure work in the marine atmospheric boundary layer, and compare these measurements to theories of wind wave growth (Equations 2-4). Section 2 describes the field site, the data collection, and the data processing. Section 3 presents the results, including comparisons between measurements and the Janssen (1999) model. Section 4 discusses the implica-

tions of these measurements for the atmospheric wave-affected boundary layer, and avenues for future work on the topic. A summary is presented in Section 5.

2 Methods

2.1 Site Description and Measurement Overview

Measurements were made from an open-lattice steel tower (Figure 1) deployed in roughly 13 m water depth in Buzzards Bay, MA. Buzzards Bay is a 48 km by 12 km basin open on the SW side to Rhode Island Sound. The average depth is 11 m, with a tide range of 1 to 1.5 m, depending on the neap/spring cycles. Winds in Buzzards Bay are frequently aligned on the long-axis (from the NE or SW), and are commonly strong, particularly in the fall and winter. The tower was deployed near the center of the bay at 41.577638 N, 70.745555 W for a spring deployment lasting from 12 April 2022 to 13 June 2022. Wind speeds were measured up to 16 m s^{-1}, and were large and sustained during a 3-day event in early May that will be the primary focus here (Figure 2, red box). A second deployment followed in the fall, extending from 22 September 2022 to 22 November 2022, which will not be discussed here.

Atmospheric measurements included three primary instrument booms that housed paired sonic anemometers (RM Young 81000RE) and high-resolution pressure sensors (Paros Scientific). The pressure sensor intakes were terminated with static pressure heads (Nishiyama & Bedard Jr, 1991), which reduce the dynamic pressure contribution to the measured (static) pressure. The tower booms were aligned at 280^o such that the NE and SW winds would be unobstructed by the tower's main body. A fourth sonic anemometer (Gill R3) was extended above the tower such that it was open to all wind directions and clear of wake by the tower structure. A single point lidar (Riegl LD90-3i) was mounted to the highest boom, such that the lidar measured the water surface elevation underneath the anemometer and pressure sensors to within a few centimeters horizontally. All instruments were time synchronized with a custom "miniNode" flux logger, that aggregated the data streams from each instrument. The heights of each instrument above the deployment mean water level are shown alongside a photograph of the tower during the spring deployment in Figure 1.

Additional atmospheric and wave measurements on the tower included short-wave and long-wave radiometers (Kipp & Zonen) a stereo camera pair (IOI 5MP Victorem),

two RH/T sensors (Vaisala), and a standard lower-resolution barometer (Setra). Additional water-side measurements were made (including temperature, conductivity, currents, turbulence, acoustic backscatter, and more) which will be described in a subsequent manuscript, and will not be used in the analysis here.

Data sampling schemes for each instrument are briefly described here. The sonic anemometers and pressure sensors were sampled continuously, with sampling frequencies 20 Hz (GIl R3) 32 Hz (RM Young, booms 1-3), 16 Hz (Paros pressure). The Lidar was nominally sampled at 20 Hz (see Appendix B for more) and sampled for 40 minutes starting at the top of each hour. Data were recorded in 20-minute long files, and timing was synchronized such that the start and end of each instrument's 20-minute files were aligned to within a few ms. The resulting time alignment between instruments was estimated to be accurate to within one instrument sample (roughly 50 ms). For short, 1 Hz waves, this timing offset would result in roughly 1 degree error in phase, with lower phase error for longer waves.

2.2 Spectral and Cross-spectral Analysis

Instruments were linearly interpolated to a 20-Hz time grid for spectral and cospectral processing. Power spectra and cross-spectra were estimated using the overlapping-segmented averaging method as implemented by MATLAB's *pwelch* and *cpsd* functions. Each time series was linearly detrended, and processed with 2048-sample windows (1.69 minutes) tapered with a Hamming window with 50% overlap between segments. The interpolation resulted in some high-frequency deviation from spectra made from the original (not interpolated) time series, although this was confined to frequencies larger than 1 Hz, above the wave-band frequencies of interest to this study. For example, interpolated sonic anemometer spectra were observed to be roughly 10-20% lower than non-interpolated spectra at 5 Hz, with no noticeable deviation at 1 Hz.

Separation of the pressure work cospectrum into wave-coherent and wave-incoherent terms for the atmospheric measurements is described in detail in Appendix A, which generally follows from previous studies and textbooks (e.g., Bendat & Piersol, 2011; Veron, Melville, & Lenain, 2008; Grare, Lenain, & Melville, 2013a). In brief, the real part of the wave-coherent cross-spectrum of p and w, $\mathrm{Re}\{G_{\tilde{p}\tilde{w}}(f)\}$, can be estimated using the power

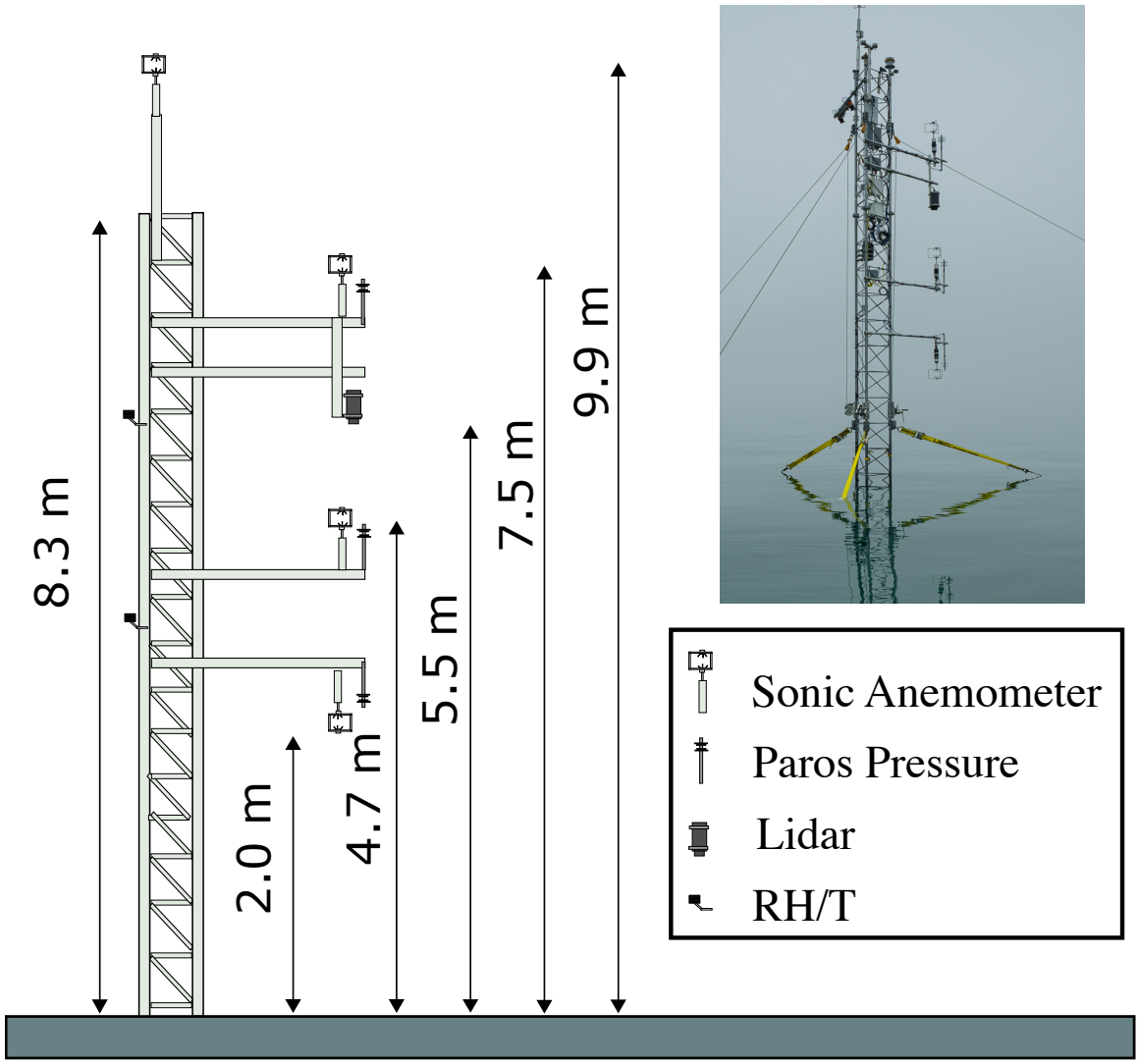

Figure 1. A schematic showing a subset of the air-side instrumentation used in this study, shown with a photograph of the tower (courtesy of S. Whelan). Heights are referenced to the tower, but represent the approximate distance to mean water level over the two month deployment. Each boom held instruments 1.2 m from the nearest tower vertical strut.

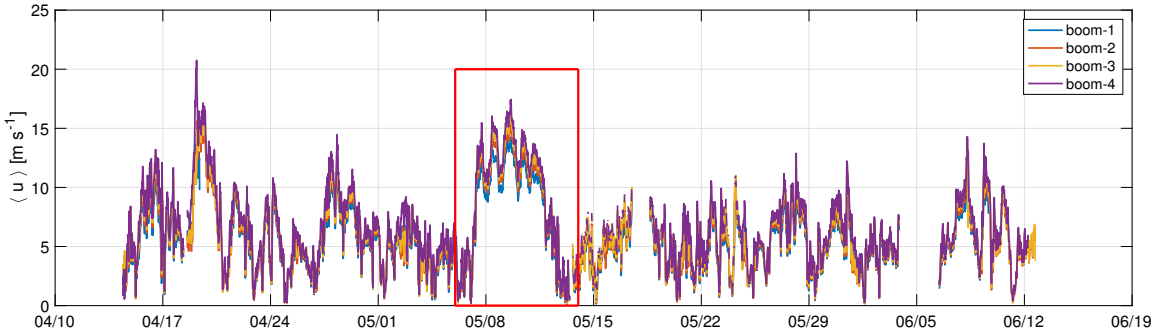

Figure 2. 20-minute mean windspeeds measured from the four vertical levels on BBASIT are shown above. A red box highlights the multi-day high winds seen in early May that are the focus of much of the analysis here.

spectrum of sea surface elevations, $G_{\eta\eta}(f)$, and the cross-spectra and phase of p and w with the sea surface respectively,

$$\mathrm{Re}\{G_{\tilde{p}\tilde{w}}(f)\} = \frac{|G_{p\eta}||G_{w\eta}|}{G_{\eta\eta}} \cos\left(\Phi_{p\eta} - \Phi_{w\eta}\right). \tag{5}$$

The total wave-coherent pressure work at measurement height can be found by integrating the above equation in frequency, $\langle \tilde{p}\tilde{w} \rangle = \int \mathrm{Re}\{G_{\tilde{p}\tilde{w}}(f)\} df$, with the integral evaluated in the wave band (between 0.1 Hz $< f <$ 2 Hz). Although somewhat arbitrary frequency bounds, it was found that choosing a lower low-frequency limit added noise in the integrated pw estimates. Increasing the high-frequency limit resulted in minor changes, but was set to where there were minimal differences between interpolated and non-interpolated spectra. Visual inspection of the magnitude squared coherence (Figure 4b) shows the most coherence at frequencies 0.2 Hz $< f <$ 0.8 Hz, well inside the chosen integration bounds.

2.3 Estimation of S_{in} and β

Wind-wave input S_{in} was estimated using the measured elevation spectrum $E(f)$, and the measured wind friction velocity u_* following Equation 4 for computation of β using the procedure described in Komen et al. (1996). Wave directions were assumed to be aligned with the local wind. This assumption is justified by the local quality of waves due to the fetch-limited environment; however we recognize that the unidirectional assumption may cause an over-estimate of S_in due to directional spreading expected in

a true spectrum. We expect ongoing analysis of subsurface data to examine this assumption in future work. Wavenumber $k(f)$ was estimated using the finite-depth linear dispersion relation, $(2\pi f)^2 = gk\sqrt{\tanh(kd)}$, where d is the local water depth, and g is the acceleration due to gravity. Due to the relatively short fetch-limited waves measured at this location, most wave frequencies were unaffected by water depth via the dispersion relation. For example, at 0.2 Hz (where there is a sharp change in coherence, Figure 4b), the finite-depth wavelength is 97% of its deep-water equivalent. Surface currents were typically less than 20 cm s^{-1}, and dispersion corrections were not considered since they are relatively small for waves at frequency $f < 1$ Hz.

3 Results

3.1 Phase-offset Pressure

During high-winds, the atmospheric pressure was found to be highly correlated and out of phase with the sea surface elevations, consistent with wind-wave growth theories (Miles, 1957; Janssen, 1991) and past measurements of wave-coherent pressure (Snyder et al., 1981; Hare et al., 1997; Donelan et al., 2005). During these events, low atmospheric pressure perturbations were seen slightly downwind of wave crests, and high atmospheric pressure perturbations were measured over wave troughs. An example is shown in Figure 3, during a high wind event that took place in early May where the lowest boomed instruments were particularly close to the wave crests. Wave-induced pressure perturbations are visible from all three booms with the pressure deviating 50-100 times the wind stress over the wave crests. Pressure perturbations were generally larger at the booms closer to the surface. Perturbations were not seen over every wave crest/trough, but were seen sporadically over groups of 5-10 sequential wave crests, particularly during high wind events.

3.2 Wave-Coherent Pressure Work

Time series of atmospheric vertical velocity showed much larger turbulence fluctuations, which make direct inspection of the relative phase with the sea surface elevations (as done for pressure in Figure 3) less clear. However cospectra of pressure work show clear negative pw in the wave band, counter to the background turbulent fluctuations which are positive (Figure 4a). Both p and w show strong coherence with waves,

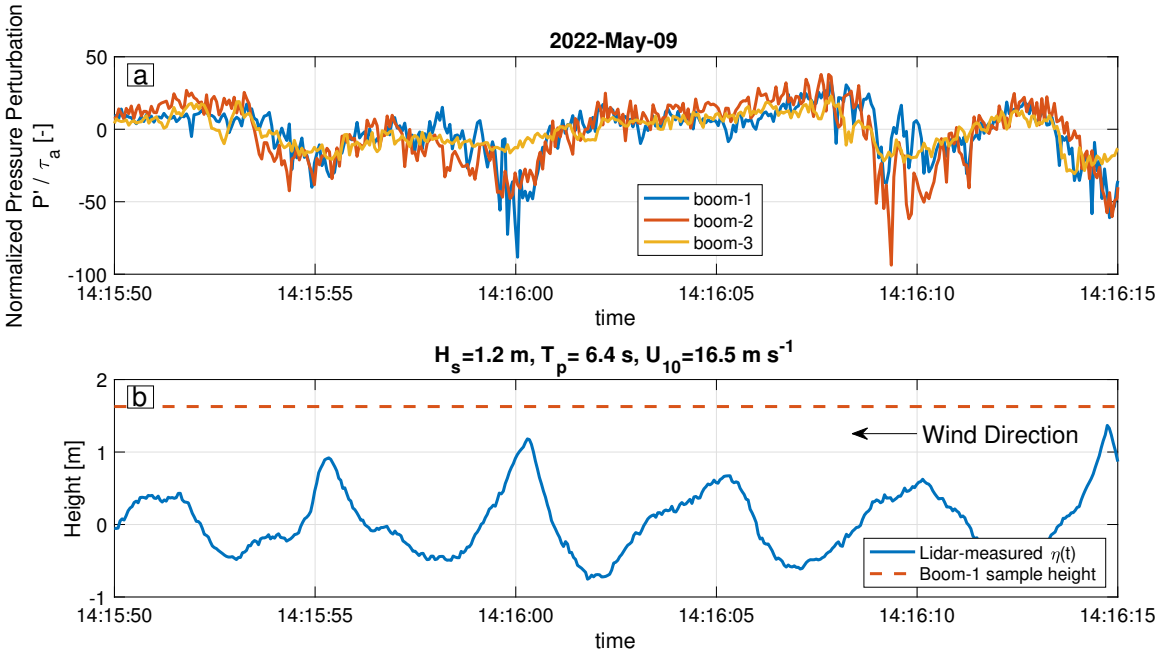

Figure 3. (a) A time series of normalized pressure perturbations measured from the three paros pressure sensors. (b) A time series of sea surface elevation measured by the single point lidar (solid blue) and the boom-1 wind and pressure sample height (dashed orange). Heights in (b) are referenced to the 20-minute mean water level. Pressure in (a) is normalized by the wind stress, estimated using a 20-minute averaging window. The pressure perturbation is the deviation from a 30-second moving average filter. Large negative atmospheric-pressure perturbations are aligned with the passage of wave crests. Waves and wind can be imagined as moving right to left in the time series, such that lidar measures the leeward (downwind) face of the wave first.

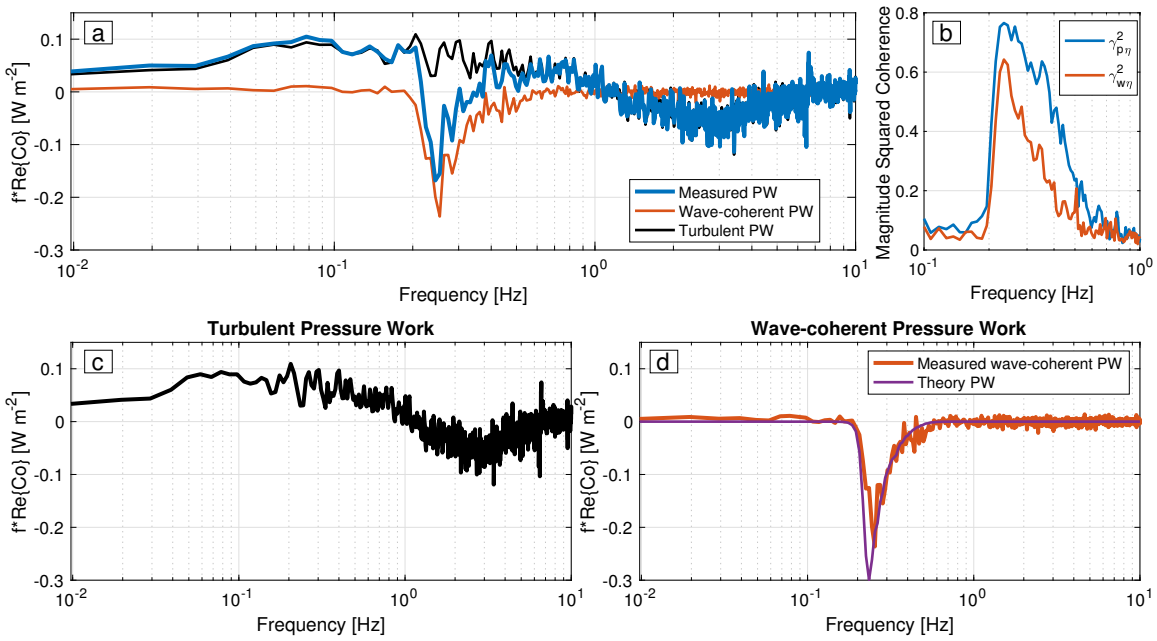

Figure 4. (a) Six 20-minute *pw* co-spectra from 9 May 2022 are averaged (blue) and shown alongside the decomposed turbulent (black, also shown in c) and wave-coherent (orange, also shown in d) components. The magnitude squared coherence, γ^2 between η and p, as well as between η and w are shown in b. There is strong coherence for pressure and vertical velocity in the wave band (0.1 Hz $< f <$ 1 Hz), which allows the decomposition shown in c and d. The Janssen (1999) model for atmospheric *pw* is shown in purple in d, which aligns well in both magnitude and shape to the measured cospectrum.

η, in the wind wave frequency band (0.05 Hz $< f <$ 1 Hz, Figure 4b), suggesting the negative *pw* is due to surface waves. A wave-turbulence decomposition (described in Appendix A) shows that the *pw* cospectrum is similar in magnitude and shape to the Janssen (1999) model (Equation 2). The spectral decay term, $\exp(-2kz)$ is essential in this fit, and the estimated surface *pw* would be both larger, and have a different spectral shape with a shift to larger values at higher frequencies.

3.3 Energy Flux Time Series

The time series of the frequency-integrated wave-coherent *pw* cospectrum is consistent with the Janssen (1999) model at the lowest boomed level over the entire high wind event, which lasted roughly 7 May 2022 to 11 May 2022. Figure 5 shows the frequency-integrated measured *pw* cospectrum against the energy fluxes estimated from the Janssen

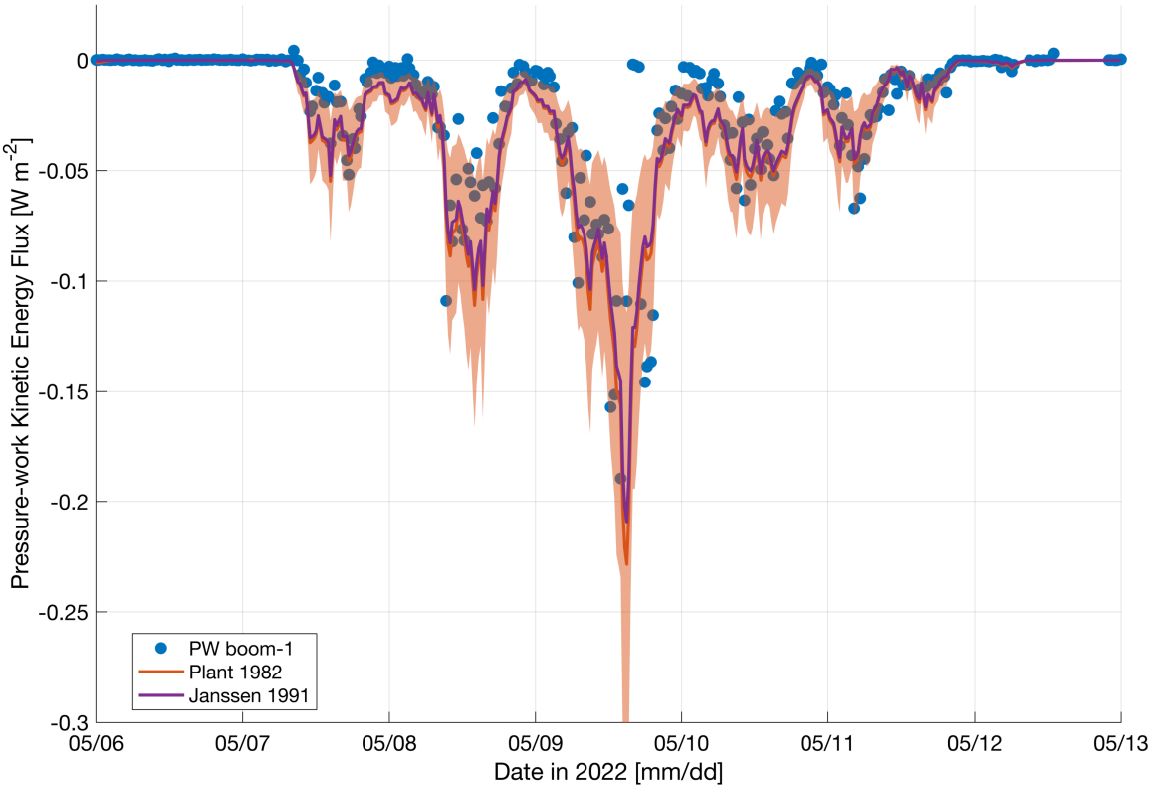

Figure 5. A comparison of the time series of wave-coherent energy fluxes estimated from measurements made from the lowest elevation boom (blue) and from the Janssen (1999) model using the Plant (1982) growth rate (orange with shaded error bars, Equation 3), and the Janssen (1991) growth rate (purple, Equation 4) over the 3-day high-wind event in early May, 2022. Error bars are derived from the reported coefficient uncertainty in Plant (1982).

(1999) model. There is good agreement in both magnitude and shape between the measurements and model, with the model slightly over-predicting energy fluxes. These results are fairly consistent if the wave growth rate β is taken from either Plant (1982) or Janssen (1991). Worse, but moderate agreement was seen at booms 2 and 3 (not shown), with much lower energy levels (0.06 W m^{-2} and 0.02 W m^{-2} respectively during the highest winds on 9 May). Curiously, the sign of the measured pressure work fluxes from the second boom was upwards on 7 May and 8 May, but not on 9 May; the cause of this sign reversal remains unexplained, and will be left to future analysis.

4 Discussion

While there is compelling consistency between the Janssen (1999) *pw* model and the pressure work measurements during this event, it is perhaps not generalizeable without more events. As noted by several authors, there is still considerable spread in existing data for growth rate, β, resulting in 50% uncertainty in the coefficient reported by Plant (1982) (as seen in Equation 3). Including this uncertainty would put the majority of measured *pw* within the uncertainty bounds in wind-wave energy flux. However, close inspection of Figure 4d shows the largest difference between the theory and measured wave-coherent pressure work occur near 0.25 Hz, just before the measured cospectrum falls off towards zero. This effect is fairly consistent across the May high-wind event, suggesting that there may be a functional difference that leads to a bias. However, it is unclear if the mismatch is due to the growth rate, the vertical decay function, the assumption of unidirectional waves, or another unidentified mechanism.

The Janssen (1999) model for atmospheric pressure work was developed as a simple way to show the drawbacks of inertial dissipation estimates of wind stress, rather than as a self-consistent theory for wind-over waves. For example, Janssen (1999) assumes potential flow for the sake of the vertical decay function which yields the $\exp(-2kz)$ term in Equation 2. However, potential flow theory is incompatible with the pressure-phase offset that leads to growth in the first place. It is somewhat remarkable then that the potential flow decay works so well and results in fairly good agreement for short waves (larger kz) at frequencies strongly modified by this decay (roughly 0.3 Hz $< f <$ 1 Hz, Figure 4d). Previous studies have shown variable decay rates for wave-induced pressure $\tilde{p}(z) = \tilde{p}(0)\exp(-\alpha kz)$ with $\alpha = 1$ for lower winds, and reaching $\alpha = 2$ for higher winds (Donelan et al., 2006). The decay in magnitude of w should be roughly equivalent to that of the pressure, such that applying the Donelan et al. (2006) pressure decay rates for $\tilde{p}\tilde{w}$ would result in a range between $\exp(-2kz)$ and $\exp(-4kz)$. However, these larger decay rates would not explain the over-estimated pressure work by the model near the wave peak, which occurs for longer waves that are less sensitive to choice of decay rate, α.

Several recent studies have also suggested variability in the wave growth rate with wave steepness as well as wave age (e.g., M. Buckley et al., 2020; Wu, Popinet, & Deike, 2022). Therefore, it could be that the spectral growth rate decreases near the peak in

relation to a roll-off in spectral steepness. Lastly, this roll-off could be due to unaccounted-for directional effects, or finite depth effects. Plant (1982) integrated a directional spreading function, which modified the unidirectional growth rate by roughly 20% (Plant, 1982 Equations 10-12 therein). Finite depth effects that modify the wave phase speed and shape of the wave orbital motions were not expected to be large, since at 5 s (the frequency where wave-coherent pressure work approaches zero in Figure 4a and d) the finite depth phase speed is still 97% that of the deep water limit.

As noted in Ayet and Chapron (2022), there is some disagreement over the expected shape of the wave-induced transport term, Π_w, which depends heavily on wave-coherent pressure work and which could impact mean wind profiles and turbulent statistics in the atmospheric boundary layer (Figure 5 therein). Very recent work from Janssen and Bidlot (2022) investigated the feedback between wave-supported energy fluxes and changes to the mean wind profile (the curvature of which sets the wave growth rate). Janssen and Bidlot (2022) found a non-linear effect was visible but relatively small at $\langle u \rangle > 15$ m s^{-1}, with a large reduction of growth rate at $\langle u \rangle = 50$ m s^{-1} which may explain the elusive drag-coefficient roll-off at high winds. We suspect continued work to understand the magnitude and decay rate of $\langle \tilde{p}\tilde{w} \rangle$ and its relation to the mean wind profile, particularly at high winds, to be a fruitful future direction of study.

4.1 Flow separation

Recent numerical and laboratory work has suggested the importance of flow separation in airflow over surface waves (Sullivan et al., 2018; M. P. Buckley & Veron, 2016; M. Buckley et al., 2020; Wu et al., 2022). In particular, Wu et al. (2022) has suggested simulations agree with the sheltering theory of Jeffreys (1924) at high winds, a theory which has largely been ignored in favor of those stemming from Miles critical layer theory. Here, we make no distinction as to the mechanism for the pressure perturbations in Figure 3, however the phase offsets were often closer to 180 degrees than to the 90 degree offset reported in Wu et al. (2022) which was used to justify sheltering theory. Still, the measurements here are made at a finite height above the surface, and there could be a change in pressure/sea-surface phase with height.

5 Conclusions

We have presented observations of wave-coherent pressure work in the wave-affected atmospheric boundary layer. Observations are qualitatively consistent with existing wind-wave growth rate parameterizations, and a vertical decay that depends on height and surface wavenumber. The vertical decay is roughly consistent with potential flow theory, which gives a vertical decay rate of $\exp(-2kz)$. The agreement between measured pressure work and existing models is seen in cospectra, and in a frequency-integrated time series over a 3-day high wind event. The simple model for atmospheric work tends to over-predict the measured pressure work by a factor of 20-50%, however this is generally within the reported error bounds of a coefficient for the wave growth parameterizations.

The pressure work energy fluxes are most easily seen at moderate to high wind speeds ($\langle u_{10} \rangle > 12$ m s^{-1}), with pressure work fluxes $\langle \tilde{p}\tilde{w} \rangle \sim 0.1$ W m^{-2}. Future work is needed to determine how these measured fluxes impact the energy budget of the wave-affected atmospheric boundary layer, and their implications for air/sea fluxes and flux measurements in energetic conditions.

Appendix A Estimation of wave-coherent and -incoherent spectra

The measured pw cospectra are decomposed using the assumption of a linear spectral model which is described here. This method closely follows Bendat and Piersol (2011) Section 6.2.2 "Single-Input/Multiple-Output Model" as well as Veron et al. (2008), and Grare et al. (2013b), in which the authors use a similar decomposition. Here, we assume that the time series of p' and w' each have a wave-coherent component, $\tilde{p}$, and $\tilde{w}$, that have a linear relationship with sea surface elevation, η, such that the Fourier Transform, $\mathcal{F}\{\cdot\}$, of each measured time series can be expressed,

$$\mathcal{F}\{p'\} = \mathcal{F}\{p'_t + \tilde{p}\} = \mathcal{F}\{p'_t\} + H_p \mathcal{F}\{\eta\} \tag{A1}$$

$$\mathcal{F}\{w'\} = \mathcal{F}\{w'_t + \tilde{w}\} = \mathcal{F}\{w'_t\} + H_w \mathcal{F}\{\eta\} \tag{A2}$$

where $\mathcal{F}\{\tilde{p}\} = H_p \mathcal{F}\{\eta\}$, and $\mathcal{F}\{\tilde{w}\} = H_w \mathcal{F}\{\eta\}$ define the wave-coherent components, p'_t and w'_t are the wave-incoherent components, and H_p and H_w are complex transfer functions that depend of frequency. Here we use notation consistent with the

measured time series, but note that the notation of Bendat and Piersol (2011) would equate to $\eta = x(t)$, $p' = y_1(t)$, and $w' = y_2(t)$, and use G_{xx} to denote the power spectrum of x, and G_{xy_1} to denote the complex cross-spectrum of x and y_1. Following Bendat and Piersol (2011)'s Equation 6.77, the complex transfer functions are defined using cross-spectra and autospectra,

$$H_p = \frac{G_{p\eta}(f)}{G_{\eta\eta}(f)}, \qquad H_w = \frac{G_{w\eta}(f)}{G_{\eta\eta}(f)}, \tag{A3}$$

where $G_{p\eta}(f)$ is the complex cross-spectrum of p' and η, $G_{w\eta}(f)$ is the complex cross-spectrum of w' and η, and $G_{\eta\eta}(f)$ is the real-valued power spectrum of η.

The cross-spectrum between p' and w', assuming no wave-turbulent correlations (e.g., $\langle \tilde{p} p'_t \rangle = 0$, $\langle \tilde{p} w'_t \rangle = 0$, etc.), is then,

$$\underbrace{G_{pw}(f)}_{Total\ pw} = \underbrace{H_p^*(f) H_w(f) G_{\eta\eta}(f)}_{Wave-Coherent\ pw} + \underbrace{G_{p'_t w'_t}(f)}_{Turbulent\ pw} . \tag{A4}$$

Since only the real component of pw correlations contribute to the TKE equation, the wave-coherent pw spectrum is estimated combining Equations A3 and A4,

$$\mathrm{Re}\{G_{\tilde{p}\tilde{w}}(f)\} = \mathrm{Re}\{H_p^*(f) H_w(f) G_{\eta\eta}(f)\} = \frac{|G_{p\eta}||G_{w\eta}|}{G_{\eta\eta}} \cos\left(\Phi_{p\eta} - \Phi_{w\eta}\right), \tag{A5}$$

where $\Phi_{pw} = \mathrm{atan}\left(\mathrm{Im}\{G_{pw}\}/\mathrm{Re}\{G_{pw}\}\right)$ is the spectral phase. The wave-incoherent part, $G_{p'_t w'_t}(f)$, is found using equations A4 and A5. Here, we followed from Bendat and Piersol (2011), however Equation A5 can also be seen as analogous to Grare et al. (2013b)'s Equation 17, which was formed for wave-coherent stress. We also note that Equation A5 can be reformed using magnitude squared coherence and auto-spectra, with magnitude squared coherence defined $\gamma_{xy}^2 = |G_{xy}|^2/(G_{xx}G_{yy})$.

The above formulation (Equation A5) is consistent with previous efforts to measure the surface wave growth rate, β, from out-of-phase pressure, $\mathrm{Im}\{G_{p\eta}\}$ (Hare et al., 1997; Donelan et al., 2006). Assuming a boundary condition where the atmospheric velocity equals the wave orbital motion at $z = 0$, we have $|G_{w\eta}(z = 0)| = \omega G_{\eta\eta}$ and $\Phi_{w\eta}(z = 0) = 90$. Combining with Equation A5,

$$\mathrm{Re}\{G_{\tilde{p}\tilde{w}}(f, z=0)\} = \frac{|G_{p\eta}|\omega G_{\eta\eta}}{G_{\eta\eta}} \cos\left(\Phi_{p\eta} - 90\right), \tag{A6}$$

which can be reduced to,

$$\mathrm{Re}\{G_{\tilde{p}\tilde{w}}(f, z=0)\} = \omega|G_{p\eta}| \sin\left(\Phi_{p\eta}\right). \tag{A7}$$

Using trig identities for phase, $|G|\sin(\Phi) = \mathrm{Im}\{G\}$, such that,

$$\mathrm{Re}\{G_{\tilde{p}\tilde{w}}(f, z=0)\} = \omega \mathrm{Im}\{G_{p\eta}\}. \tag{A8}$$

Acknowledgments

This work was funded by NSF Award Number 2023020. Jay Sisson and Steve Faluotico helped design, deploy, maintain, and recover the tower and associated measurement systems. Thanks to Jonah Mikutowicz and the AGM and 41^o North crews for invaluable help with deployment and recovery of the tower. Al Plueddemann, Tim Duda, Chris Zappa, and Alejandro Cifuentes-Lorenzen provided helpful comments and discussions.

Open Research

Data used in this work (Zippel et al., 2022) is available through the WHOI Open Access Server (WHOAS) at DOI: 10.26025/1912/29583. Code used to process data and produce figures will be made available on Github at the time of publication.

References

Ayet, A., & Chapron, B. (2022). The dynamical coupling of wind-waves and atmospheric turbulence: a review of theoretical and phenomenological models. *Boundary-Layer Meteorology*, *183*, 1–33.

Belcher, S., & Hunt, J. (1993). Turbulent shear flow over slowly moving waves. *Journal of Fluid Mechanics*, *251*, 109–148.

Bendat, J. S., & Piersol, A. G. (2011). *Random data: analysis and measurement procedures* (Vol. 729). John Wiley & Sons.

Buckley, M., Veron, F., & Yousefi, K. (2020). Surface viscous stress over wind-driven waves with intermittent airflow separation. *Journal of Fluid Mechanics*, *905*.

Buckley, M. P., & Veron, F. (2016). Structure of the airflow above surface waves. *Journal of Physical Oceanography*, *46*(5), 1377–1397.

Cifuentes-Lorenzen, A., Edson, J. B., & Zappa, C. J. (2018). Air–sea interaction in the southern ocean: Exploring the height of the wave boundary layer at the air–sea interface. *Boundary-Layer Meteorology*, *169*(3), 461–482.

Donelan, M. A., Babanin, A. V., Young, I. R., & Banner, M. L. (2006). Wave-follower field measurements of the wind-input spectral function. part ii: Parameterization of the wind input. *Journal of physical oceanography*, *36*(8), 1672–1689.

Donelan, M. A., Babanin, A. V., Young, I. R., Banner, M. L., & McCormick, C. (2005). Wave-follower field measurements of the wind-input spectral function. part i: Measurements and calibrations. *Journal of Atmospheric and Oceanic Technology*, *22*(7), 799–813.

Grare, L., Lenain, L., & Melville, W. K. (2013a). Wave-coherent airflow and critical layers over ocean waves. *Journal of Physical Oceanography*, *43*(10), 2156–2172.

Grare, L., Lenain, L., & Melville, W. K. (2013b, 2013/12/11). Wave-coherent airflow and critical layers over ocean waves. *Journal of Physical Oceanography*, *43*(10), 2156–2172. Retrieved from `http://dx.doi.org/10.1175/JPO-D-13-056.1` doi: 10.1175/JPO-D-13-056.1

Hara, T., & Belcher, S. E. (2004). Wind profile and drag coefficient over mature ocean surface wave spectra. *J. Phys. Oceanogr.*, *34*(11), 2345–2358.

Hare, J. E., Hara, T., Edson, J. B., & Wilczak, J. M. (1997). A similarity analysis of the structure of airflow over surface waves. *Journal of Physical Oceanography*, *27*(6), 1018–1037.

Hristov, T. S., Miller, S. D., & Friehe, C. A. (2003). Dynamical coupling of wind and ocean waves through wave-induced air flow. *Nature*, *422*, 55-58.

Janssen, P. A. (1989). Wave-induced stress and the drag of air flow over sea waves. *Journal of Physical Oceanography*, *19*(6), 745–754.

Janssen, P. A. (1991). Quasi-linear theory of wind-wave generation applied to wave forecasting. *Journal of physical oceanography*, *21*(11), 1631–1642.

Janssen, P. A. (1999). On the effect of ocean waves on the kinetic energy balance and consequences for the inertial dissipation technique. *Journal of physical oceanography*, *29*(3), 530–534.

Janssen, P. A., & Bidlot, J.-R. (2022). Wind-wave interaction for strong winds.

Journal of Physical Oceanography.

Jeffreys, H. (1924). On the formation of waves by wind. *Proc. R. Soc. London*, *A107*, 189-206.

Jeffreys, H. (1925). On the formation of waves by wind. ii. *Proc. R. Soc. London*, *A110*, 341-347.

Komen, G. J., Cavaleri, L., Donelan, M., Hasselmann, K., Hasselmann, S., & Janssen, P. (1996). *Dynamics and modelling of ocean waves*.

Miles, J. W. (1957). On the generation of surface waves by shear flows. *Journal of Fluid Mechanics*, *3*(2), 185–204.

Nishiyama, R. T., & Bedard Jr, A. J. (1991). A "quad-disc"static pressure probe for measurement in adverse atmospheres: With a comparative review of static pressure probe designs. *Review of scientific instruments*, *62*(9), 2193–2204.

Phillips, O. M. (1957). On the generation of waves by turbulent wind. *Journal of fluid mechanics*, *2*(5), 417–445.

Pizzo, N., Deike, L., & Ayet, A. (2021). How does the wind generate waves? *Physics Today*, *74*(11), 38–43.

Plant, B. (1982). A relationship between wind stress and wave slope. *J. Geophys. Res.*, *87*, 1961-1967.

Snyder, R., Dobson, F., Elliott, J., & Long, R. (1981). Array measurements of atmospheric pressure fluctuations above surface gravity waves. *Journal of Fluid mechanics*, *102*, 1–59.

Sullivan, P. P., Banner, M. L., Morison, R. P., & Peirson, W. L. (2018). Turbulent flow over steep steady and unsteady waves under strong wind forcing. *Journal of Physical Oceanography*, *48*(1), 3–27.

Veron, F., Melville, W. K., & Lenain, L. (2008). Wave-coherent air–sea heat flux. *Journal of physical oceanography*, *38*(4), 788–802.

Wu, J., Popinet, S., & Deike, L. (2022). Revisiting wind wave growth with fully coupled direct numerical simulations. *J. Fluid Mech.*, *951*(A 18). doi: 10.1017/jfm .2022.822

Zippel, S. F., Edson, J. B., Scully, M. E., & Keefe, O. R. (2022, December). *Dataset:"data to accompany "direct observation of wave-coherent pressure work in the atmospheric boundary layer".* https://hdl.handle.net/1912/29583. doi: DOI:10.26025/1912/29583

Figure 2.

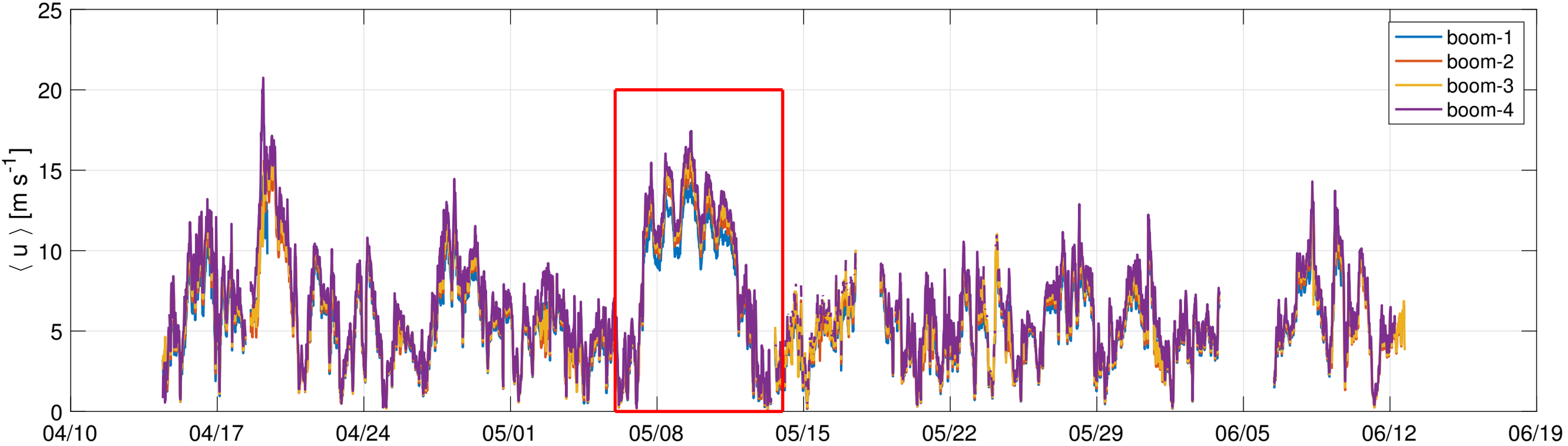
boom-1
boom-2
boom-3
boom-4
⟨ u ⟩ [m s-1]
0
5
10
15
20
25
04/10
04/17
04/24
05/01
05/08
05/15
05/22
05/29
06/05
06/12
06/19

Figure 3.

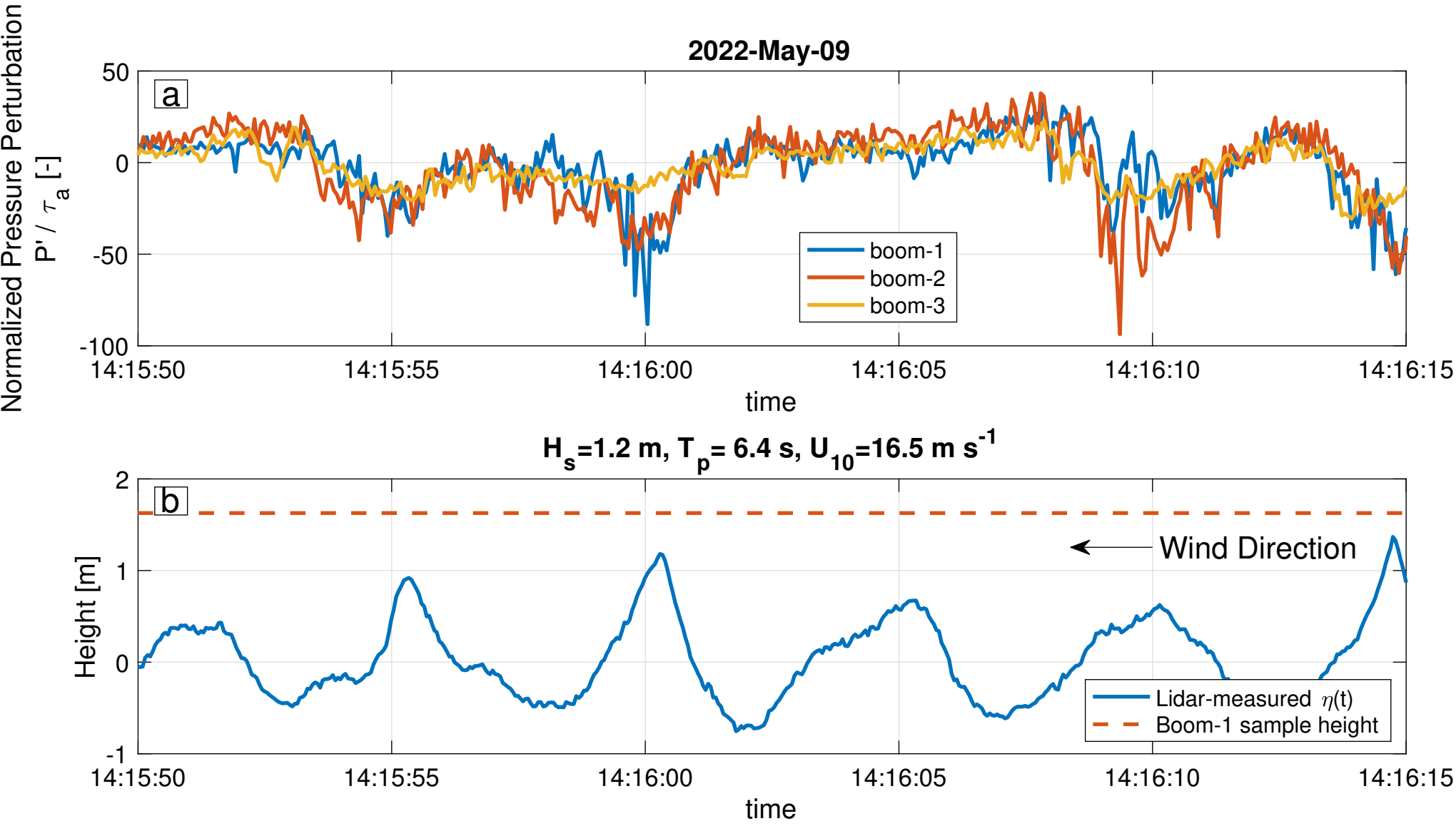
2022-May-09
a
Normalized Pressure Perturbation
P' / τa [-]
50
0
-50
-100
boom-1
boom-2
boom-3
14:15:50
14:15:55
14:16:00
14:16:05
14:16:10
14:16:15
time
Hs=1.2 m, Tp= 6.4 s, U10=16.5 m s-1
b
Height [m]
2
1
0
-1
Wind Direction
Lidar-measured η(t)
Boom-1 sample height
14:15:50
14:15:55
14:16:00
14:16:05
14:16:10
14:16:15
time

Figure 4.

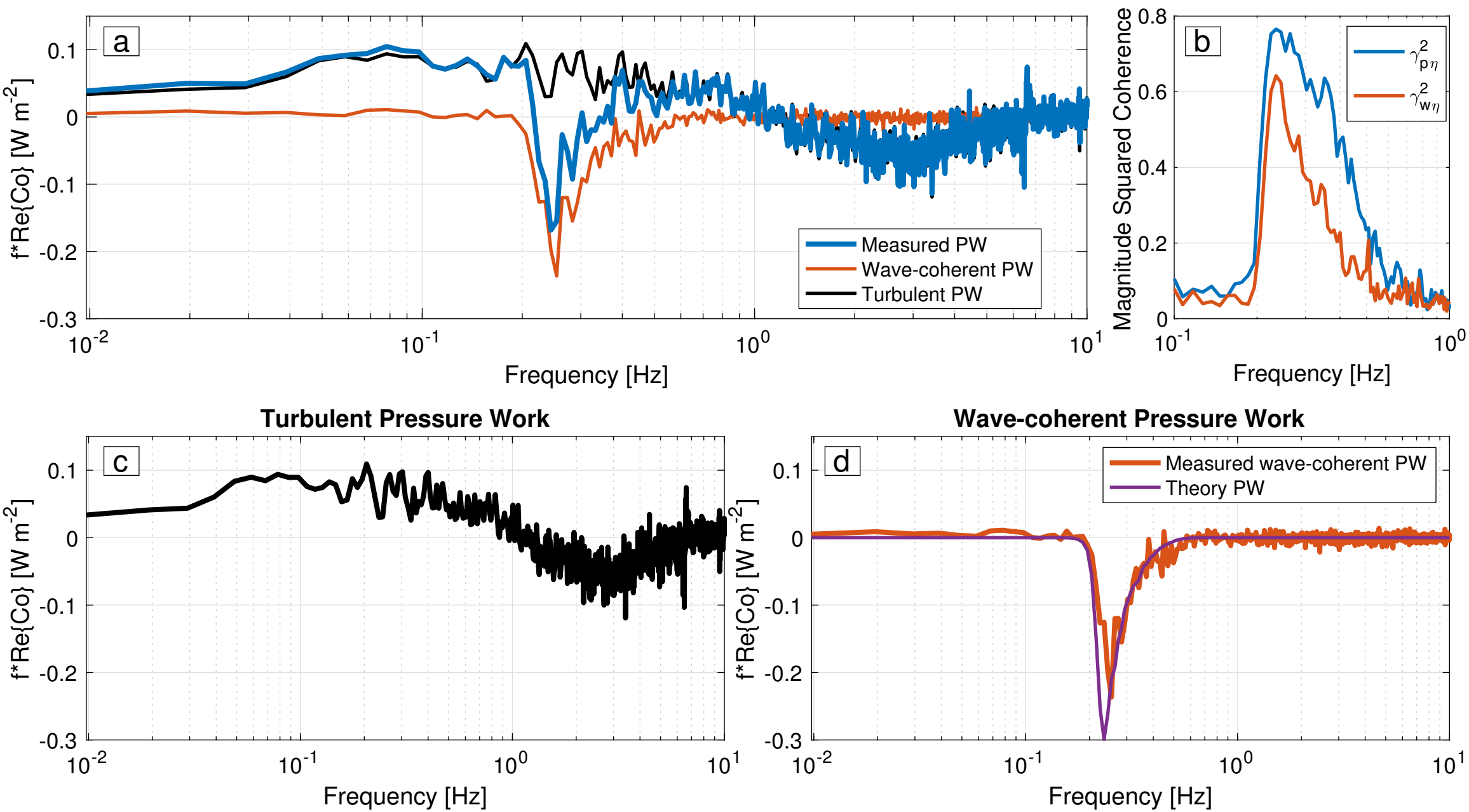
a
f*Re{Co} [W m-2]
Frequency [Hz]
Measured PW
Wave-coherent PW
Turbulent PW
b
Magnitude Squared Coherence
Frequency [Hz]
Turbulent Pressure Work
c
f*Re{Co} [W m-2]
Frequency [Hz]
Wave-coherent Pressure Work
d
Measured wave-coherent PW
Theory PW
f*Re{Co} [W m-2]
Frequency [Hz]

Figure 5.

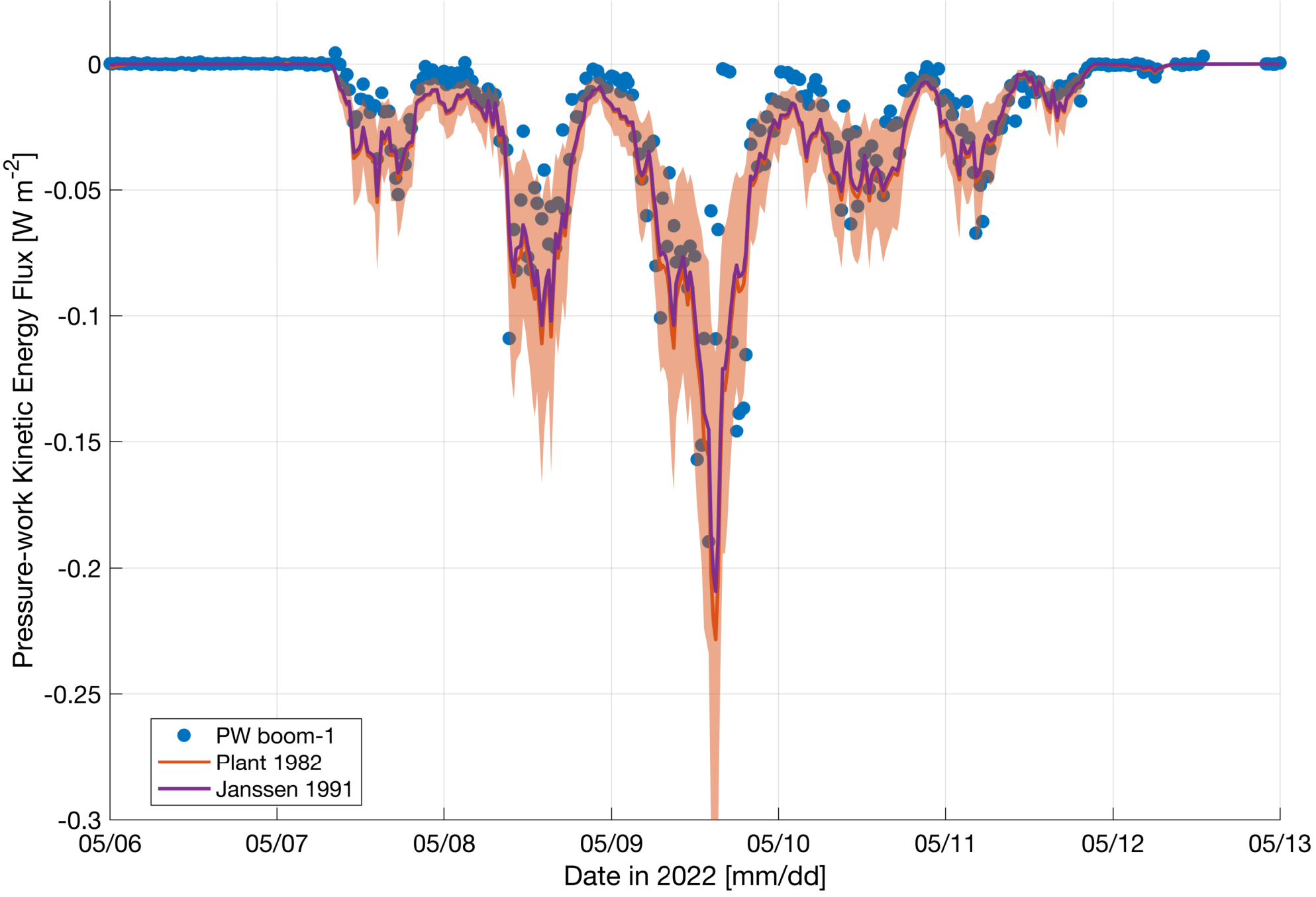
0
-0.05
-0.1
-0.15
-0.2
-0.25
-0.3
Pressure-work Kinetic Energy Flux [W m-2]
05/06
05/07
05/08
05/09
05/10
05/11
05/12
05/13
Date in 2022 [mm/dd]
PW boom-1
Plant 1982
Janssen 1991